COMMON-REFLECTION-SURFACE-BASED WORKFLOW FOR DIFFRACTION IMAGING

S. Dell and D. Gajewski

email: *sergius.dell@zmaw.de*

keywords: *CRS-based diffraction imaging*

ABSTRACT

Imaging of diffractions is a challenge in seismic processing. Standard seismic processing is tuned to enhance reflections. Separation of diffracted from reflected events is frequently used to achieve an optimized image of diffractions. We present a method to effectively separate and image diffracted events in the time domain. The method is based on the Common-Reflection-Surface-based diffraction stacking and the application of a diffraction-filter. The diffraction-filter uses kinematic wavefield attributes determined by the Common-Reflection-Surface approach. After the separation of seismic events, poststack time migration velocity analysis is applied to obtain migration velocities. The velocity analysis uses a semblance based analysis of diffraction traveltimes. The procedure is incorporated into the conventional Common-Reflection-Surface workflow. We apply the procedure to 2D synthetic and field data. The application of the method to simple and complex synthetic data revealed promising results. A marine field data example shows a less good separation of reflections and diffractions which might be due to the higher frequency content of the data and a less aggressive choice in the filter parameters because of a complex geological setting with rugged top of salt and faults.

INTRODUCTION

The main effort in seismic processing techniques is to enhance reflection events. Diffracted waves are usually considered as noise and often suppressed in the pre-processing. However, reflected waves are not suitable for high-resolution structural imaging, i.e., imaging of features beyond the classical Rayleigh limit of half a seismic wavelength (Khaidukov et al., 2004; Moser and Howard, 2008). Typical examples are small-size scattering objects, pinch-outs, fracture corridors, and karst structures. Imaging and monitoring of these features can be essential for the geological interpretation. Diffracted waves allow to detect and image such local heterogeneities (Landa et al., 1987; Landa and Keydar, 1997). Diffracted waves may also indicate the presence of faults and are essential in their investigations (Krey, 1952; Kunz, 1960). Moreover, diffractions can serve as quality control for velocity models in migration methods. Conventional migration methods use only reflections. The velocity model is consistent with the data if seismic events in common-image-gathers (CIG) are flat. However, a velocity model is also consistent with the data if the primary diffractions are focused to points. Velocity analysis based on diffractions focusing may be used to determine migration velocities instead of CIG flatness analysis (Sava et al., 2005). The reflection imaging may also profit from proper imaging of diffractions. The attenuation of diffracted noise, e.g., from shallow sea bed, can be achieved by subtraction of the corresponding diffractions from the total recorded data (Necati et al., 2005).

To enhance diffraction imaging a first step is to separate diffractions from reflections. The separation can be based on the attenuation of specular reflections in the recorded wavefield and may be performed in time or depth domain. Separation in depth domain is most suitable for complex media, however, a very well determined velocity model is required. For models with moderate velocity variations, the separation in the time domain is more robust with respect to the quality of velocity model.

Several methods have been developed to separate diffractions in the time domain. Fomel et al. (2006) and Taner et al. (2006) used plane-wave destruction filters to separate diffractions in the time domain. The filters are prediction-error filters based on an implicit finite-difference scheme for the local plane-wave equation (Harlan et al., 1984). The criterion for separating diffracted and reflected events is the smoothness and continuity of local event slopes that correspond to reflection events. Berkovitch et al. (2009) proposed another algorithm for diffraction imaging in time. Their method is based on the summation of diffracted events using the multifocusing operator. The diffraction multifocusing stack separates diffracted and reflected energy in the stacked section by focusing diffractions and smearing the reflection energy over a large area.

In this paper, we introduce a workflow for diffraction imaging based on the 2D Common-Reflection-Surface (CRS) approach (Müller, 1999; Mann, 2002). The purpose of this work is to incorporate diffraction imaging in the conventional CRS workflow and time migration velocity analysis using diffractions. The presented event separation algorithm combines the coherent summation of diffracted events and the reflection attenuation via the diffraction filter. The main difference to diffraction imaging by multifocusing proposed by Berkovitch et al. (2009) is the separation of the seismic events in the poststack data domain using CRS attributes and the incorporation of the method into the CRS workflow (Baykulov et al., 2010) without the need for additional parameter searches.

THEORY

Common-Reflection-Surface method

The basic idea of the CRS stack method (Jäger et al., 2001; Höcht, 2002; Bergler, 2004; Hertweck et al., 2007) is to use a second-order approximation of the squared traveltime in the vicinity of the normal ray as a stacking trajectory

$$t_{hyp}^2(m,h) = \left(t_0 + 2\,p_m\,m\right)^2 + 2t_0\left(M_N\,m^2 + M_{NIP}\,h^2\right), \tag{1}$$

where m is the midpoint displacement with respect to the considered CMP position m_0, h is half source-receiver offset, t_0 corresponds to the ZO two-way traveltime, and p_m, M_N, M_{NIP} are stacking parameters that define the shape of the CRS trajectory. $p_m = \partial t/\partial m$ is the first-order horizontal spatial traveltime derivative with respect to the midpoint coordinate or horizontal slowness. $M_N = \partial^2 t/\partial m^2$ is the second-order horizontal spatial traveltime derivative with respect to midpoint coordinate. $M_{NIP} = \partial^2 t/\partial h^2$ is the second-order horizontal spatial traveltime derivative with respect to the half-offset coordinate. In the following we also use the phrase *operator* if we refer to a stacking trajectory.

The stacking parameters p_m, M_N, and M_{NIP} contain information on the kinematics of the recorded wavefield. Physically, these parameters can be interpreted as attributes of two hypothetical wavefronts emerging at the measurement surface location m_0 (Hubral, 1983). The parameter p_m corresponds to the slowness of the ZO normal ray emerging at m_0. It is related to the emergence angle β_0 (see Figure 1a)

$$p_m = \frac{\sin\beta_0}{v_0}, \tag{2}$$

where v_0 is the near-surface velocity. The parameter M_{NIP} is related to the curvature of a wavefront emerging at m_0 when a point source is placed at the Normal-Incident-Point (NIP) of the reflector. The associated wave is called the NIP-wave. The relation for M_{NIP} reads

$$M_{NIP} = \frac{\cos^2\beta_0}{v_0} K_{NIP}\,, \tag{3}$$

where K_{NIP} is the wavefront curvature of the NIP-wave (Figure 1b).

The parameter M_N is related to the curvature of a wavefront emerging at m_0 from an exploding reflector element, the Common Reflection Surface, centered at the NIP. As all rays associated with this wave are locally normal to the reflector element in the subsurface, it is called the normal wave. The relation for M_N reads

$$M_N = \frac{\cos^2\beta_0}{v_0} K_N\,, \tag{4}$$

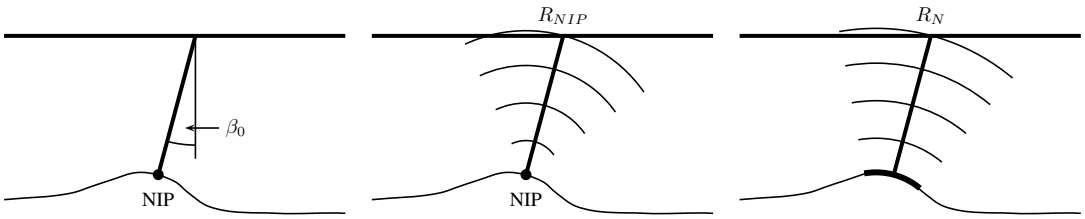

(a) Emergence angle

(b) Point source experiment at the NIP with K_{NIP} as curvature in the measurement surface

(c) Exploding CRS centered at the NIP with K_N as curvature in the measurement surface

Figure 1: The physical meaning of the kinematic wavefield attributes β_0, K_{NIP} and K_N.

where K_N is the wavefront curvature of the normal wave (Figure 1c).

Wavefront curvatures can be expressed through their radii $K_N = 1/R_N$ and $K_{NIP} = 1/R_{NIP}$. The curvatures, or the radii, and the angle of emergence represent the kinematic wavefield attributes or CRS attributes. Inserting p_m, M_N, and M_{NIP} expressed by the CRS attributes in equation 1 provides the CRS stacking operator as

$$t^2_{hyp}(m,h) = \left[t_0 + \frac{2\,\sin\beta_0}{v_0}m\right]^2 + \frac{2\,t_0\cos^2\beta_0}{v_0}\left[\frac{m^2}{R_N} + \frac{h^2}{R_{NIP}}\right]. \tag{5}$$

The kinematic wavefield attributes may be used for a number of applications, including the calculation of geometrical spreading (Hubral, 1983), the determination of the approximated projected Fresnel zones (Mann, 2002), depth velocity model building with NIP-wave tomography (Duveneck, 2004), limited-aperture depth migration (Jäger, 2004), generalized Dix-type inversion (Müller, 2007), CRS-based time migration (Spinner, 2007), prestack data regularization and enhancement (Baykulov and Gajewski, 2009), or multiple suppression (Dümmong, 2010).

In the following section, we discuss the use of CRS attributes to separate diffractions from reflections.

Diffraction imaging with the Common-Reflection-Surface method

In a homogeneous medium, where the rays are straight lines, the diffraction traveltime can be computed by the double-square-root (DSR) operator. The DSR operator can be obtained by a simple application of Pythagoras theorem and reads

$$t_D = \sqrt{\frac{t_0^2}{4} + \frac{(m-h)^2}{v^2}} + \sqrt{\frac{t_0^2}{4} + \frac{(m+h)^2}{v^2}}, \tag{6}$$

where h is half source-receiver offset, m is the midpoint displacement with respect to the considered CMP position m_0, t_0 corresponds to the vertical zero-offset two-way traveltime, and v is the time migration velocity.

The straight-line assumption is not valid for inhomogeneous media. However, we can generalize the DSR operator using a Taylor expansion, where we assume local smoothness of traveltimes in the vicinity of the image ray. The image ray is normal to the registration surface (Hubral, 1977). The local smoothness assumption implies that the velocity in the vicinity of the image ray shows moderate lateral change. This limitation is a result of the hyperbolic assumption, i.e., the expansion up to second order. For heterogeneous media, the DSR operator requires the same assumptions as the CRS operator for reflections.

According to the CRS theory, a diffractor is associated to a reflector segment with an infinite curvature and an undefined orientation (Mann, 2002). A reflector segment with infinite curvature implies that $R_N = R_{NIP}$ or $M_N = M_{NIP}$, respectively. As opposed to reflections, for diffractions any direction describes a possible zero-offset ray along which the NIP-wave and N-wave can be considered. For a diffractor every emerging ray is a 'normal' ray.

If the kinematic wavefield attributes for an arbitrary point in the data are known, an approximation of the prestack diffraction response is available by simply substituting R_{NIP} for R_N or vise versa in Equation 5, i.e.,

$$t^2 = \left[t_0 + \frac{2\,\sin\beta_0 m}{v_0}\right]^2 + \frac{2\,t_0\cos^2\beta_0}{v_0 R_{NIP}}\left[m^2 + h^2\right]. \tag{7}$$

Equation 7 represents the CRS-based diffraction (CRSD) operator which approximates the diffraction response up to second-order. The CRSD traveltime surface is a hyperboloid in (t, m, h) space which is obtained by rotating a hyperbola around its semi-minor axis. The CRSD operator assigns the stacked result to the stationary point of the traveltime surface with respect to (m, h), which coincides with the ZO time t_0 of the 'normal' ray. The DSR operator assigns the stacked result to the operator apex which coincides with the ZO time of the image ray. The CRSD operator does not focus the diffractions to their apex but represents a fit to the traveltime based on a coherence criterion.

The CRSD operator is a single-square root operator which coincides with the DSR operator for zero-offset, i.e., for $h = 0$. For offsets greater zero, the DSR traveltime surface and the CRSD traveltime surface deviate from each other, as seen in Figure 2. Only near offset sections should be considered for diffractions. Please note that Figure 2 resembles the homogeneous case. For heterogeneous media, both operators are valid in the hyperbolic limit. It cannot be quantified which operator may fit the data better since it is model dependent. To keep the offset small will improve the fit for both operators though.

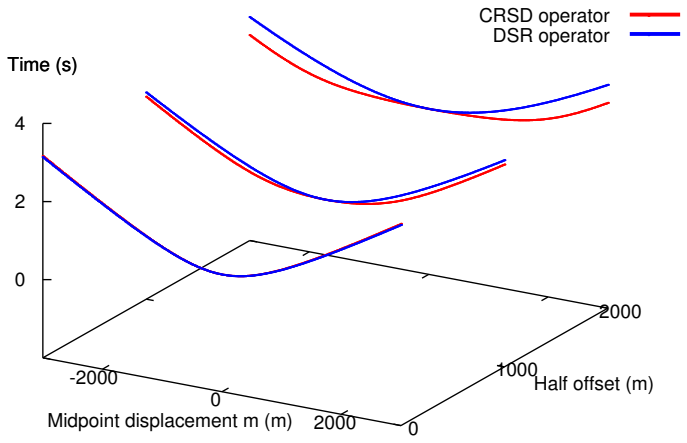

Figure 2: Double-square-root (DSR) and CRS-based diffraction (CRSD) operator for a 2D homogeneous model with a single diffractor at a depth of 1.1 km. The velocity is 1500 m/s. The operators coincide in the plane defined by $m = 0$ and $h = 0$, respectively. The larger the offset, the more the operators deviate from each other. Offsets far above the diffractor depth are considered.

It was mentioned above that the radii of curvature of the NIP-wave, R_{NIP}, and normal wave, R_N, coincide for diffractions. Thus, the ratio of R_{NIP} and R_N can be used to identify diffracted events (Mann, 2002). In the ideal case, a diffractor should yield a ratio of R_{NIP}/R_N equal to one. Strictly speaking, this applies to the high frequency limit since the operators are kinematic. Seismic data are always band limited and do not allow such easy distinction. Moreover, R_{NIP} and R_N are determined from data using an approximation to the real traveltime and it is not possible to determine diffractions in a binary way, i.e., $R_N = R_{NIP}$ is diffraction and $R_N \neq R_{NIP}$ is reflection. A soft transition is required which can be achieved by thresholding. This transition should display a smooth and fast decay in order to sufficiently separate diffractions from reflections. We suggest the following function which serves as a guide for

thresholding:

$$T_F(m_0, t_0) = e^{-\frac{|R_N - R_{NIP}|}{|R_N + R_{NIP}|}}. \tag{8}$$

This function is about one for R_{NIP} close to R_N and rather small if R_{NIP} and R_N differ.

Since the radii of curvature may slightly differ for a diffracted event, we use a threshold determined from the function $T_F(m_0, t_0)$ to stabilize the filter process. We weight the stacked result with one if the function $T_F(m_0, t_0)$ is above the threshold and with zero in the opposite case. The choice of the threshold depends on the complexity of the subsurface and the spectral content of the data. The lower the threshold, the more residual reflections will remain in the data. The application of the designed filter to poststack sections will not include reflected events in the stack because they have a lower value of $T_F(m_0, t_0)$. Diffracted events will remain in the stack because they have a higher value of $T_F(m_0, t_0)$. The resulting stacked section will then contain predominantly diffraction energy.

Subsurface structures with small radii of curvature with respect to the prevailing wavelength in the signal may appear very similar to diffraction events. Events from these structures will pass the filtering process and interfere with diffractions. In conflicting dip situations, reflected and diffracted events contribute to the same ZO location while they have different kinematic wavefield attributes. The kinematic wavefield attributes of both events should be considered to proper separate the seismic events. We propose to use an extended CRS stack strategy as described by Mann (2002) to avoid this potential problem. The strategy allows to detect conflicting dip situations estimating kinematic wavefield attributes separately. All attributes are then used for the filtering process.

Depending on the value of the threshold, residual reflections may be present in the resulting stack. These reflections may still have greater amplitudes than diffractions and the diffraction amplitudes may be distorted by the filtering process in conflicting dip situations. To enhance the diffraction amplitudes and suppress the residual reflections, we apply the CRSD operator to the poststack section utilizing partial CRS stack (Baykulov and Gajewski, 2009). For a sample with a certain CMP and time coordinate, we calculate the diffraction traveltime curve using the poststack CRSD stack operator given by

$$t^2 = \left[t_0 + \frac{2\,\sin\beta_0}{v_0} m\right]^2 + \frac{2\,t_0\cos^2\beta_0}{v_0 R_{NIP}} m^2, \tag{9}$$

and stack the amplitudes within a large midpoint aperture. For a point belonging to the residual reflected event, the poststack CRSD operator will stack the amplitudes coherently only in the vicinity of the stationary point. Thus, stacking along a large diffraction trajectory will sum up both coherent and incoherent events. The residual reflected events will be further suppressed because of the destructive interference. For a point belonging to the diffracted event, the CRSD operator stacks the amplitudes coherently along the whole diffraction trajectory. The diffracted event will be enhanced because of constructive interference.

After separating diffractions from reflections, we can use the diffraction-only data for a poststack velocity analysis

Poststack time migration velocity analysis

The conventional stacking velocity analysis is tuned to reflections. The velocity analysis applied here is tuned to diffractions and is based on a coherence analysis for diffraction traveltimes. We use the semblance norm as a measure of the coherence (Taner and Koehler, 1969). The diffraction traveltimes are computed by the zero-offset DSR operator which for $h = 0$ simplifies to

$$t_D = \sqrt{t_0^2 + \frac{4m^2}{v^2}}\,. \tag{10}$$

We perform a velocity scan from low to high velocities evaluating the semblance value for each sample in the stacked section. The output is a coherence map which is suitable for picking time migration velocities. The final migration velocity model is obtained by spline interpolation between picked locations.

Since the DSR operator is defined at its apex time, the coherence analysis will provide the highest semblance value for the correct migration velocity and for the apex location of the diffraction traveltime. This additional information can be used in the stacking procedure. The CRS approach assumes the continuous

surface around the NIP. That means that for the NIP located in the nearest vicinity of the fault, edge, or truncations, the CRS approach may results in a smeared image. The midpoint aperture of the CRS operator should be restricted in this case such that the diffracting subsurface feature is not included into the aperture. In other words, the stacking aperture should either start or terminate at the diffracting element, i.e., faults, edge, or pinch out. In the velocity analysis of the diffraction-only data, we identify the apex position of the diffracting subsurface feature that allows us to apply optimized CRS apertures which will exclude these regions.

EXAMPLES

In this section, we apply the method to separate seismic events and build time migration velocity models from poststack diffraction data. We present applications to synthetic data for a simple and complex model, and to field data .

Synthetic model with four diffractions

Figure 3a displays a stacked section of a synthetic model containing five layers and four small lenses which simulate diffractors. The velocity within the layers is constant. The velocity in the first layer is 1500 m/s, in the second layer 1580 m/s, in the third layer 1690 m/s, in the fourth layer 1825 m/s, and in the fifth layer 2000m/s. Four small lenses with a lateral extension of 200 meters in the fourth layer produce diffractions. We used Seismic Un*x to generate synthetic seismograms with the Gaussian beam method applying a Ricker-wavelet with a prevailing frequency of 25 Hz.

The following processing steps were performed: (1) the extended pragmatic search strategy to estimate the CRS attributes (Mann, 2002); (2) stacking of the prestack data using the CRSD operator to emphasize diffractions; (3) application of the diffraction filter to the stacked section to further suppress reflected events; (4) poststack partial CRSD stack to enhance diffraction amplitudes and attenuate residual reflected events (Baykulov and Gajewski, 2009). The resulting stacked section contains predominantly diffraction energy (Figure 3b). However, the pragmatic search strategy may not lead to an optimum diffraction imaging result. The search does not involve supergathers and may miss global coherence maximum. Although a global optimization is applied as a final step, the CRS stack still may not provide the best fit to diffraction events. The separation will be poor when the attributes are poor.

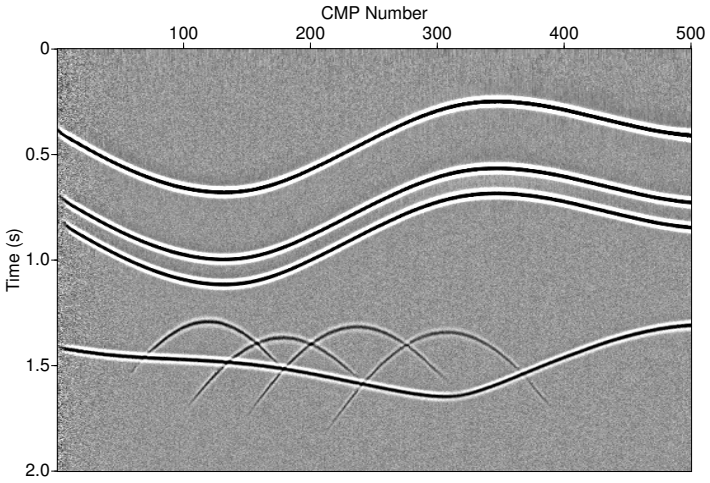

(a)

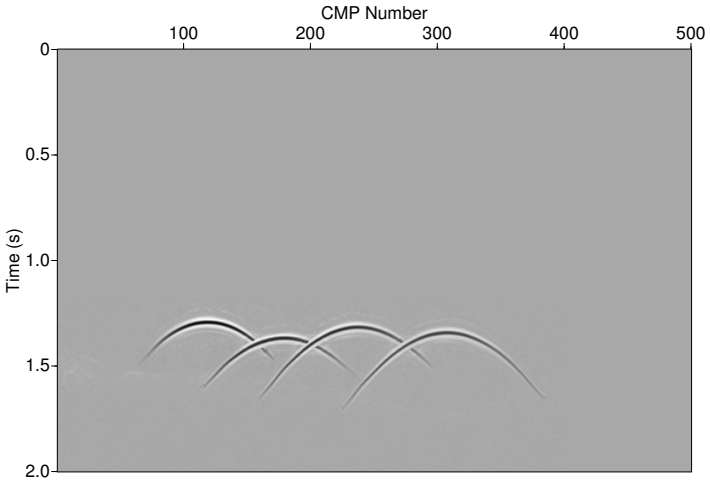

(b)

Figure 3: Synthetic example with four small lenses of 200 m lateral extension simulating diffractions. Stacked section of the recorded wavefield (a) and diffraction-only data (b). Lateral extension of the seismic line is 6250 m. Good separation of seismic events has been achieved. Conflicting dips with respect to the horizontal reflection events are preserved.

We used 0.9 as a threshold for the filter. Inverting the formula for the threshold function given by Equation 8 with respect to the ratio R_{NIP}/R_N provides

$$\frac{R_{NIP}}{R_N} = \frac{1+\ln(T_F)}{1-\ln(T_F)}\,.$$

The threshold of 0.9 for the filter corresponds to $R_{NIP} \approx 0.8R_N$. As can be observed in Figure 3b the diffracted events are well separated from the reflected events, even in regions of conflicting dips.

The diffraction-only data were then used for poststack time migration velocity analysis. Figure 4a illustrates a migration-velocity panel for CMP 120, i.e., above the most left diffractor. Figure 4b shows the

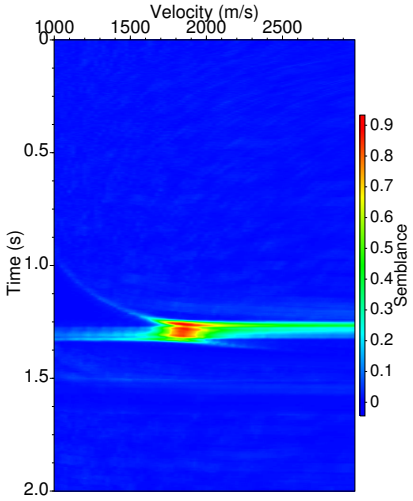

(a)

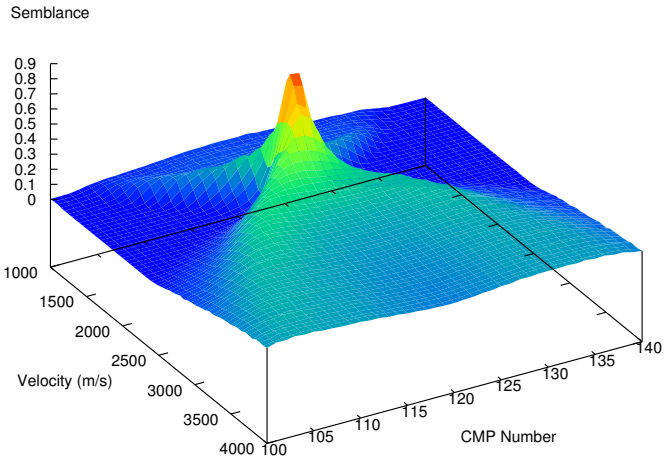

(b)

Figure 4: Velocity analysis for the synthetic model with four small lenses. (a) velocity spectrum after poststack time migration velocity analysis of CMP 120. Red color indicates high semblance. The corresponding distribution of the coherence as function of velocity for the same CMP is illustrated in (b). The time was manually picked and corresponds to the maximum of the coherence value at 1.29 s. We observe a sharp and narrow maximum with high coherence (~ 0.9) for the diffraction apex indicating a good fit to the data.

coherence values as a function of velocity and CMP position. We observe a sharp and narrow maximum for the apex of the diffraction. The time in Figure 4b was manually picked and corresponds to the maximum of the coherence value in Figure 4a. Figure 5 shows the time-migrated sections obtained by Kirchhoff poststack time migration using RMS velocities (a) and time migration velocities estimated from diffraction-only data (b). The RMS velocities were obtained by converting the CRS attributes to stacking velocities. To remove high-frequency outliers, the RMS velocities were smoothed using an event-consistent approach (Mann and Duveneck, 2004). The diffractions are focused at the lenses in both cases. The lateral extent of

the imaged diffractions is smaller in the example using velocities determined from diffraction-only data.

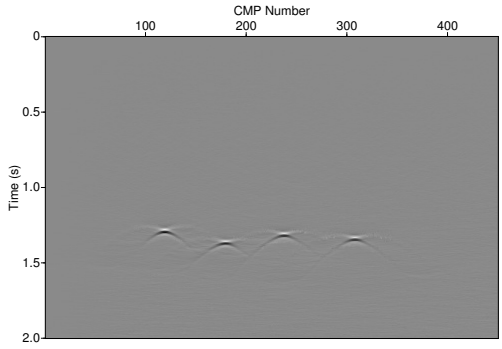

(a)

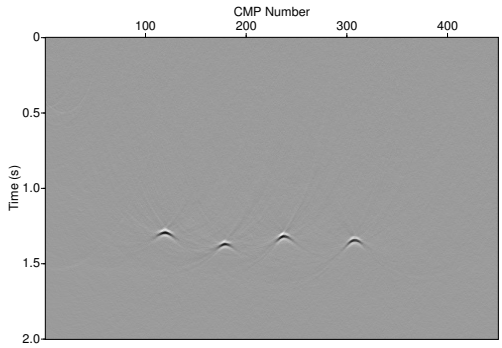

(b)

Figure 5: Imaging of the synthetic example with four small lenses. (a) Poststack time migration of the diffraction-only data obtained by using RMS velocities determined from CRS attributes and (b) using velocities estimated from the diffraction-only data.

Complex synthetic data: Sigsbee2A

After testing our method on the simple synthetic model, we apply it now to the more complex Sigsbee2A synthetic model. It is a constant density acoustic data set released in 2001 by the Subsalt Multiple Attenuation Team Joint Venture (SMAART JV). The SMAART JV has created several 2D synthetic data sets. One of the objectives was to better understand the imaging issues contributing to the poor S/N ratio observed subsalt in deepwater environments such as the Sigsbee Escarpment in the Gulf of Mexico (Fig. 6).

Figure 7a shows the stacked section of the data. Topography of the top of salt as well as faults cause strong diffractions in the right part of the section. The diffractions in the left part of the section are mostly caused by diffractors. Figure 7b illustrates the stacked section after the application of seismic event separation. A threshold of 0.9 was used for the filter. The reflected events are strongly attenuated, e.g., in the left part of the section.

The seismic event separation is controlled by the value of the threshold function. The high level of the threshold leads to quite an aggressive filtering of the data. Consequently, the reflections are strongly attenuated, however, some diffractions like events may also not pass the filtering, especially diffractions from the regions of the base of salt. In such areas, the hyperbolic assumption does not hold and the estimated radii of curvature may strongly vary for diffracted events. Decreasing the threshold leads to more residual reflections remaining in the diffraction-only data. A potential improvement may be obtained

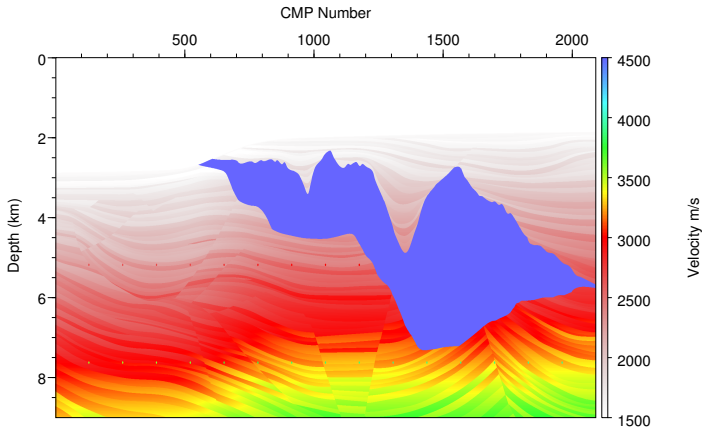

Figure 6: Synthetic Sigsbee2A example: The model reveals the rough topography of the top of salt, complex fault systems, and a great number of diffractors in subsalt and areas without salt coverage.

by a time varying thresholding.

Time migration velocity analysis was applied to the diffraction-only data (Fig. 8). With the estimated velocity model we performed poststack Kirchhoff time migration. Figure 9 shows the time-migrated image of the diffraction-only data. The diffractions in the left part of the section are focused to diffractors (Fig. 9a). In the right part of the section, the diffractions are focused to sharp edges of the rugged top of salt body (Fig. 9b).

Field data

After applications to synthetic data, we applied the developed method for diffraction imaging to field data. It is a 2D marine data set from the south-eastern Mediterranean Sea with a complex geological settings. A subset of the data consisting of 2000 CMP gathers with a total line length of $\sim$15 km, a shot spacing of 25 m, a receiver spacing of 12.5 m, and maximum offsets of 7325 m was chosen. The record length was 8 s with 4 ms sample rate.

Figure 10a shows the stacked section of the recorded data up to 5 seconds. Diffracted events, that occur along the top of salt, indicate a fractured structure. Figure 10b shows the stacked section after the diffraction separation. Because of the complexity of the data we used a low threshold of 0.7 during the filtering. Consequently, more residual reflections are present in the stacked section in comparison to the synthetic examples shown before. However, the reflection events between the seafloor and top of salt are strongly attenuated leaving well-imaged diffraction events from the top of salt.

We applied time migration velocity analysis to the diffraction-only data (Fig. 11) and then performed poststack Kirchhoff time migration with the estimated velocity model. Figure 12a shows the time-migrated image of the recorded data. Figure 12b shows the time-migrated image of the diffraction-only data. The diffractions are focused to the small rugged elements of the top of salt and indicate its rough topography.

DISCUSSION AND CONCLUSIONS

We have proposed a method to separate reflections and diffractions using CRS attributes. The process consists of stacking of the coherent events with a CRS-based diffraction operator followed by attenuation of reflected events in the poststack domain with a new type of filter. This filter is based on CRS attributes which were determined by the CRS approach. No additional analysis or search is required. In a post processing step, the diffraction amplitudes are enhanced using partial CRS stacks. A subsequent time migration velocity analysis on the diffraction-only data provides time migration velocities which are then

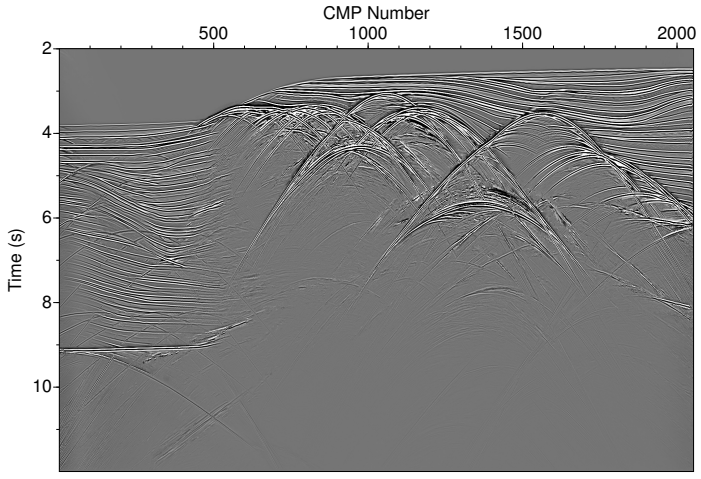

(a)

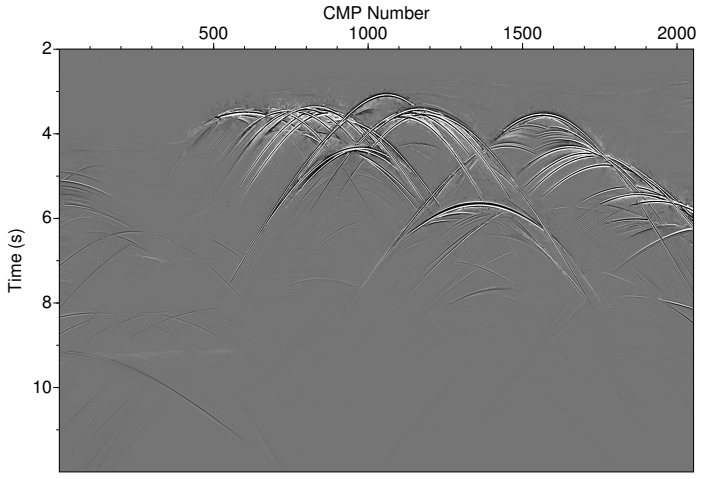

(b)

Figure 7: Results for the synthetic Sigsbee2A model. Stacked section of the recorded wavefield (a) and diffraction-only data (b).

used for Kirchhoff poststack time migration.

The radii of the normal and NIP-wave allow to identify seismic events. For diffractions, both radii should coincide, i.e., their ratio is close to one. We used an exponential threshold function instead of the simple ratio to stabilize the filter process and to allow for a smooth transition from diffractions to reflections. The choice of the threshold controls the separation of seismic events and depends on the complexity of the subsurface as well as on the frequency content of the data. The lower the threshold, the more residual reflections will remain in the diffraction-only data. Because of possible distortion of the diffraction amplitudes in conflicting dip areas during the filtering, we apply a partial CRS stack for an enhancement of the diffractions.

The diffraction-only data can be used for a poststack time migration velocity analysis. In the poststack domain, the data are reduced and a good S/N ratio is present. This allows fast time migration velocity

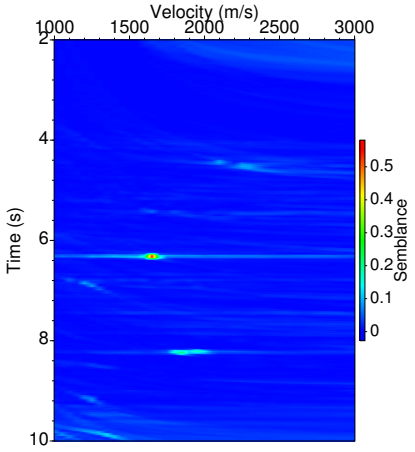

(a)

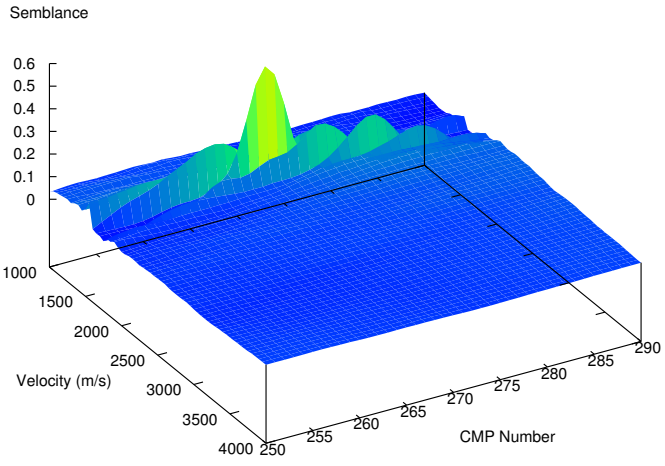

(b)

Figure 8: (a) Velocity analysis for CMP 268 of the Sigsbee2A model. This CMP location is right above a diffractor location (see Fig. 6). The corresponding distribution of the coherence for the CMP is illustrated in (b). The time was manually picked and corresponds to the maximum of the coherence value at about 6.3 s. We observe a sharp and narrow maximum for the diffraction apex.

analysis. The velocity analysis consists of a velocity scan for each CMP location and the evaluation of the corresponding semblance norm.

Applications of the method to synthetic and field data data demonstrate that the presented separation of seismic events followed by the time migration velocity analysis leads to well focused diffractions. The developed filter is not limited to stacking trajectories. The application to prestack data is also possible. Moreover, the extension of the method to 3D is straightforward. Diffraction imaging is an inherently 3D problem since we can not expect the diffractors to be located below our profile. The 2D examples presented in this paper illustrate the functioning of the process though.

The field data example showed higher residual reflected energy compared to the synthetic 2D examples. This may well be a 3D effect of diffractors located transverse to the profile line. Another possible

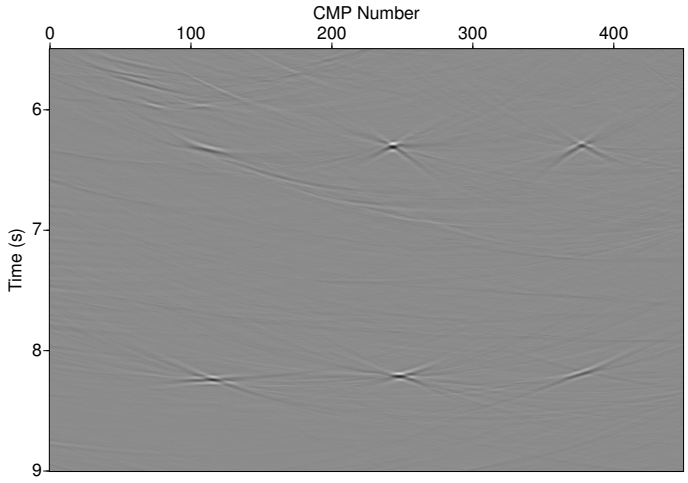

(a)

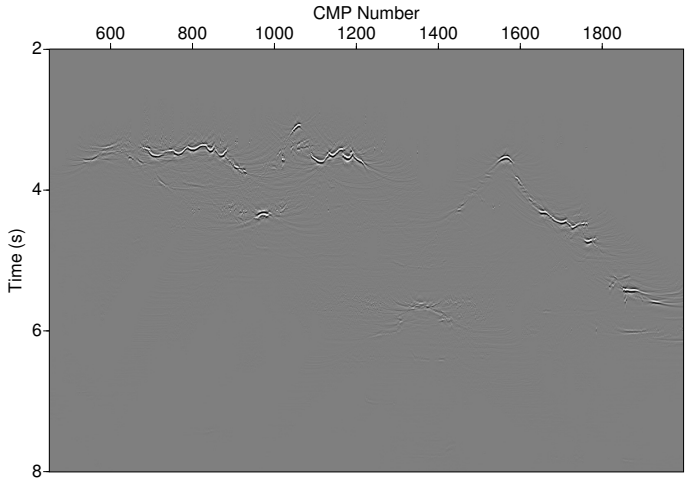

(b)

Figure 9: Imaging of Sigsbee2A data. Poststack time migration of the diffraction-only data for the left part of the model (a) and the right part of the model (b). In the left part of the model diffractions are focused to diffractors. However, because of residual reflections we observe tails around diffractors. In the right part of the model the diffractions are caused by the rugged geometry of the top of salt. After the poststack time migration, the focused diffractions reveal the top of salt complexity.

explanation of this observation could be the frequency content of the data. The field data example contains considerably higher frequencies in the signal spectrum than the synthetic data. Imaging with diffractions and to distinguish reflections and diffractions is frequency dependent. What might appear as a "point diffractor" to a low frequency signal may well be a "reflecting horizon" for a high frequency signal. The corresponding Fresnel volume defines the limits of resolution here. The frequency content of the data thus highly influences the filter performance. The same threshold in the filter process will not provide the same performance with respect to the separation of diffraction and reflection events if the frequency content of the data differs.

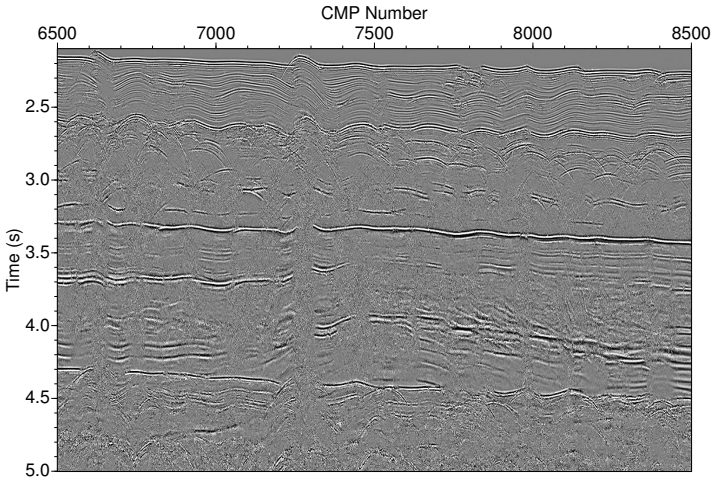

(a)

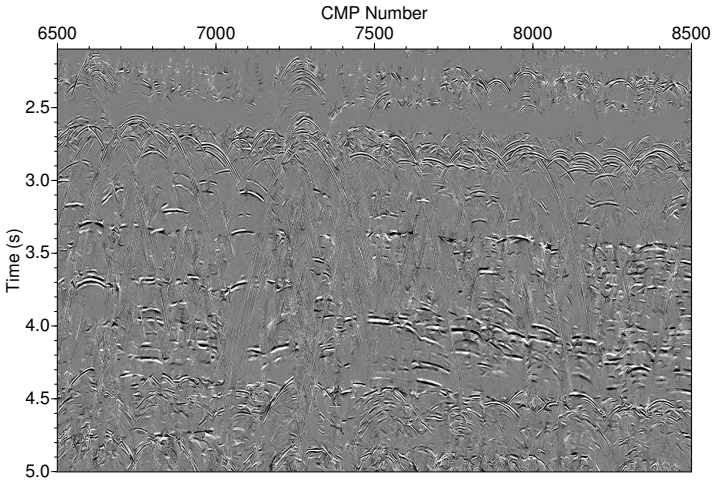

(b)

Figure 10: Marine data from the Levantine Basin. (a) Automatic CMP stacked section of the recorded wavefield. (b) CRSD stacked section of diffraction-only data. Reflections are still present in (b), because of the lower threshold we have chosen for the threshold function.

ACKNOWLEDGMENTS

We would like to thank the sponsors of WIT consortium for their support. We are grateful to the Applied Geophysics Group Hamburg, Boris Kashtan from St. Petersburg State University, Russia, Evgeny Landa from OPERA, France, and Martin Tygel from UNICAMP, Brazil, for continuous discussions. We also thank SMAART JV consortium and TGS for kindly providing the data.

REFERENCES

Baykulov, M., Dümmong, S., and Gajewski, D. (2010). From time to Depth with CRS attributes. *Geophysics*, page revised.

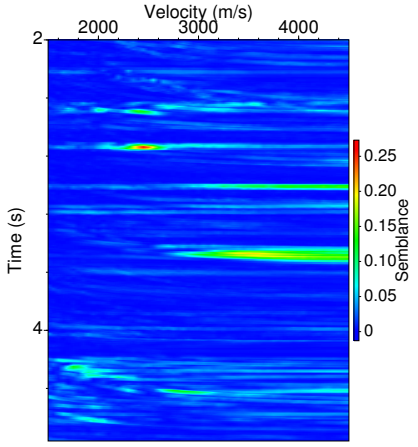

(a)

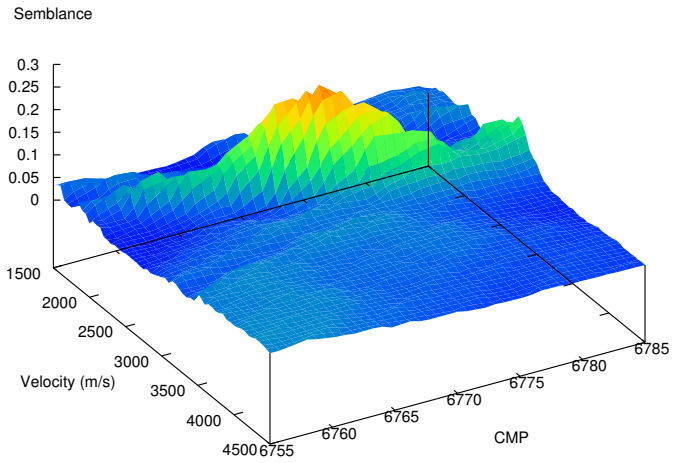

(b)

Figure 11: Marine data from the Levantine Basin. (a) Velocity spectrum after poststack time migration velocity analysis of CMP 6771 located directly above the diffractor. (b) Coherence of this CMP where the time was manually picked and corresponds to the maximum of the coherence value at 2.87 s in (a). The semblance is considerably smaller compared to the synthetic examples. A distinct maximum can be still identified.

Baykulov, M. and Gajewski, D. (2009). Prestack seismic data enhancement with partial common-reflection-surface (CRS) stack. *Geophysics*, 74:no. 3, V49–V58.

Bergler, S. (2004). *On the determination and use of kinematic wavefield attributes for 3D seismic imaging*. Logos Verlag, Berlin.

Berkovitch, A., Belfer, I., Hassin, Y., and Landa, E. (2009). Diffraction imaging by multifocusing. *Geophysics*, 74:no. 6, WCA75–WCA81.

Dümmong, S. (2010). *Seismic data processing with an expanded Common Reflection Surface workflow*. PhD thesis, University of Hamburg.

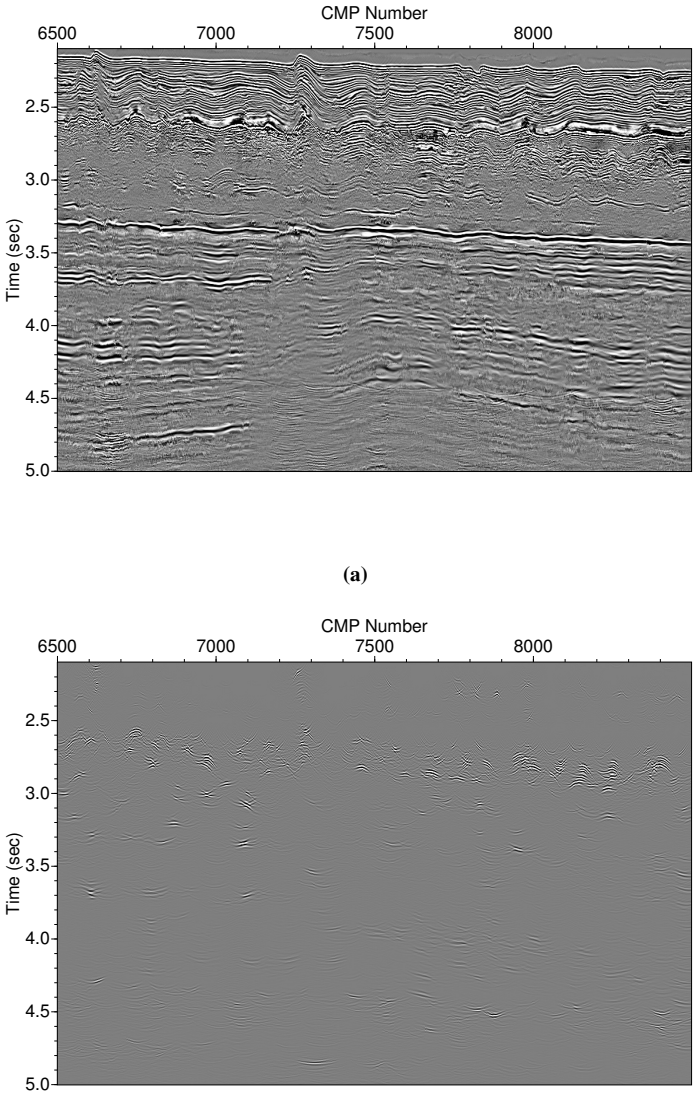

Figure 12: Marine data from the Levantine Basins. Time-migrated sections: (a) obtained with the estimated RMS velocities and (b) obtained with the velocities estimated from the diffraction-only data. The diffractions are focused and indicate the rough topography of the top of salt. Combining both time images improves the overall image of the subsurface.

Duveneck, E. (2004). *Tomographic determination of seismic velocity models with kinematic wavefield attributes*. Logos Verlag Berlin.

Fomel, S., Landa, E., and Taner, M. T. (2006). Posstack velocity analysis by separation and imaging of seismic diffractions. *Geophysics*, 72:no. 6, U89–U94.

Harlan, W. S., Claerbout, J. F., and Rocca, F. (1984). Signal/noise separation and velocity estimation. *Geophysics*, 49:1869–1880.

Hertweck, T., Schleicher, J., and Mann, J. (2007). Data stacking beyond CMP. *The Leading Edge*, 26(7):818–827;DOI:10.1190/1.2756859.

Höcht, G. (2002). *Traveltime approximations for 2D and 3D media and kinematic wavefield attributes*. PhD thesis, University of Karlsruhe.

Hubral, P. (1977). Time migration – Some ray theoretical aspects. *Geophysical Prospecting*, 25:738–745.

Hubral, P. (1983). Computing true amplitude reflections in a laterally inhomogeneous earth. *Geophysics*, 48:1051–1062.

Jäger, R. (2004). *Minimum aperture Kirchhoff migration with CRS stack attributes*. PhD thesis, University of Karlsruhe.

Jäger, R., Mann, J., Höcht, G., and Hubral, P. (2001). Common-reflection-surface stack: Image and attributes. *Geophysics*, 66:97–109.

Khaidukov, V., Landa, E., and Moser, T. J. (2004). Diffraction imaging by focusing-defocusing: An outlook on seismic superresolution. *Geophysics*, 69:1478–1490.

Krey, T. (1952). The Significance of Diffraction in the Investigation of Faults. *Geophysics*, 17:843–858.

Kunz, B. F. J. (1960). Diffraction problems in fault interpretation. *Geophysical Prospecting*, 8:381–388.

Landa, E. and Keydar, S. (1997). Seismic monitoring of diffraction images for detection of local heterogeneities. *Geophysics*, 63:1093–1100.

Landa, E., Shtivelman, V., and Gelchinsky, B. (1987). A method for detection of diffracted waves on common-offset sections. *Geophysical Prospecting*, 35:359–373.

Mann, J. (2002). *Extensions and Applications of the Common-Reflection-Surface Stack Method*. Logos Verlag Berlin.

Mann, J. and Duveneck, E. (2004). Event-consistent smoothing in generalized high-density velocity analysis. *SEG expanded abstracts*, 23:2176.

Moser, T. J. and Howard, C. B. (2008). Diffraction imaging in depth. *Geophysical Prospecting*, 56:627–641.

Müller, N.-A. (2007). *Determination of interval velocities by inversion of kinematic 3D wavefield attributes*. PhD thesis, TH Karlsruhe.

Müller, T. (1999). *Seismic imaging without explicit knowledge of the velocity model*. PhD thesis, TH Karlsruhe.

Necati, G., Magesan, M., and Connor, J. (2005). Diffracted noise attenuation in shallow water 3D marine surveys. *SEG expanded abstracts*, 24:2138.

Sava, P. C., Biondi, B., and Etgen, J. (2005). Wave-equation migration velocity by focusing diffractions and reflections. *Geophysics*, 70:no. 3, U19–U27.

Spinner, M. (2007). *CRS-based minimum-aperture Kirchhoff migration in the time domain*. PhD thesis, University of Karlsruhe.

Taner, M. and Koehler, F. (1969). Velocity-spectra digital computer derivation and applications of velocity functions. *Geophysics*, 34:859–881.

Taner, M. T., Fomel, S., and Landa, E. (2006). Prestack separation of seismic diffractions using plane-wave decomposition. In *76th Annual International Conference, SEG*, pages 2401–2404. Expanded Abstracts.